A lubricated tribocorrosion model incorporating surface roughness

Shoufan Cao [a], Stefano Mischler [b],*

[a] Nanjing University of Science and Technology, School of Mechanical Engineering, 210094 Nanjing, Jiangsu, China
[b] Ecole Polytechnique Fédérale de Lausanne (EPFL), Tribology and Interface Chemistry Group (SCI-STI-SM), Station 12, CH-1015 Lausanne, Switzerland

A R T I C L E   I N F O

A B S T R A C T

This study presents an improvement of an existing tribocorrosion model developed for passive CoCrMo alloys. This model is based on an empirical formalism established by Duncan Dowson in his pioneering works on the relation between wear and elasto-hydrodynamic lubrication. The improvement consists in introducing surface topography features allowing for a mechanistic relation between lubrication and wear. The effective normal force accounting for the plastic deformation of passive metals during lubricated tribocorrosion was described through the real contact area, which in turn was related to the worn surface topography (roughness) and the elasto-hydrodynamic film thickness. The modified model was applied to results from dedicated tribocorrosion experiments obtained by varying the lubricant viscosity and the contacting surface roughness. Good correlations were found between the mechanical and chemical wear rates and corresponding variables, which validated the model. Further development of the model should include boundary film effects, third bodies build-up and time dependent evolution of the worn surface.

1. Introduction

Tribocorrosion, i.e. the degradation resulting from the combined action of wear and corrosion, has been increasingly investigated in the past years due mainly to its relevance for biomedical implants and in the marine field [1–6]. Among materials classes, passive metals such as stainless steels, CoCrMo and Ti alloys have been widely studied in tribocorrosion due to their widespread technological application in corrosive environments [5]. Experimental investigations highlighted the crucial role played by the interactions of mechanical and chemical phenomena in tribocorrosion. The interaction assumes different forms. For example, sliding can remove the passive film from the metal surface and thus enhances corrosion. On the other hand, the electrochemical conditions are known to affect the mechanical response of the metal surface to friction. [5,6]. Modeling of the tribocorrosion of passive films has been recently reviewed [7]. Tribocorrosion was mathematically described using analytical and numerical models. Analytical models present the advantage of being simple and directly relating degradation to well defined experimental parameters. As a drawback, they essentially address steady state conditions and can hardly address time dependent effects that are best described using numerical approaches. Among the analytical models, the one proposed by Cao et al. [8] is the most comprehensive in terms of mechanisms as it takes into account not

only wear and corrosion aspects, but also the role of fluid lubrication in the mixed lubrication regimes usually encountered in tribocorrosion. Indeed, in tribocorrosion, often very smooth worn surfaces are generated through tribochemical processes. Therefore, even thin fluid films can have a significant lubricating effect reducing the load carried by asperities. The close interaction of elasto-hydrodynamic effects and wear was first evidenced by Dowson et al. in the case of self-mated CoCrMo alloy artificial hip joints tested in simulators [9]. Dowson et al. [9] presented an empirical equation describing wear as being inversely proportional to the hydrodynamic minimum film thickness (at the power 1.49) as calculated using the Hamrock-Dowson equation [10].

The formalism of Cao's model is based on the assumption (already proposed by Uhlig in 1954 [11]) that the total material degradation in tribocorrosion consists in the sum of mechanical wear (removal of metallic particles) and chemical wear (removal of oxidized metal). Then, mechanical wear and chemical wear can be modelled separately.

The total wear for passive metals in sliding contacts can finally be described by Eq. (1) by considering Archard [12] mechanical wear empirical model and the wear accelerated corrosion model developed by Mischler et al. [13] and several other researchers [14–18]:

* Corresponding author.
E-mail address: stefano.mischler@epfl.ch (S. Mischler).

$$V_{tot} = V_{mech} + V_{chem} = k_m \left(\frac{F_n}{H}\right) v_s + k_c \frac{Q_p M v_s}{nF\rho} \left(\frac{F_n}{H}\right)^{0.5} \qquad (1)$$

where, V_{tot} is the total wear rate, V_{mech} is the mechanical wear rate, V_{chem} is the chemical wear rate, F_n is the normal force, H is the surface hardness, v_s is the sliding velocity, Q_p is the passivation charge density, M is the molecular mass, n is the charge number, F is the Faraday's constant, ρ is the density of the metal, k_m and k_c are the mechanical and chemical factors, respectively.

Recently, Cao et al. [8] incorporated the lubrication aspect into the tribocorrosion model in Eq. (1) by considering that the hydrodynamic fluid film in between the contacting asperity junctions reduces the normal force carried by the contacting asperities (called effective normal force F_{eff}) and thus alleviates wear [9]. Due to the lack of mechanistic description of the F_{eff}, it was related to the F_n empirically (Eq. 2) using a correlation extracted from the running-in wear of CoCrMo MoM hip implants featured with relatively smooth surfaces (Ra < 50 nm) [9] tested in hip joint simulators.

$$F_{eff} = k_0 \frac{F_n}{(h_{min})^{1.49}} \qquad (2)$$

where, h_{min} is the minimum hydrodynamic film thickness and k_0 is a proportionality factor. The model was found to predict with good precision the wear rate of CoCrMo alloys tested in tribometers and the running–in wear rate observed in MoM artificial hip joints [19,20].

Due to the empirical correlation (Eq. 2) used in this model to relate the effective normal force to total normal force, the model is in principle restricted to CoCrMo alloys. In addition, surface roughness has been found to be a crucial parameter influencing the lubrication of sliding contacts and thus wear while the model is limited to mirror polished surface finishing. The applicability of this model to other materials and contacts with different surface roughness is still an open question, The verification of the above two factors should be based on a large database and thus a lot of experimental work.

This study was initiated with the aim to develop a mechanistic approach to describe the effective normal force based on the worn surface topography (roughness). This general approach will overcome the limitation of Cao's model regarding the empirical correlation between wear and hydrodynamic film thickness used to describe the effective normal force. Finally, the model will be compared to dedicated experimental results to assess the validity of the model.

2. Modeling

2.1. Real Contact Surface in Lubricated Condition

In mixed lubricated contact, the nominal contact is composed of asperity junctions and the hydrodynamic fluid film in between. The basic principle to account for the lubrication effect in Cao's model [8] is that, the total normal force applied to the whole contact is carried by both of the contacting asperities and the hydrodynamic film. Only the force carried by the contacting asperities, which is called effective normal force (F_{eff}), causes plastic deformation of the metal and consequently induces wear. As a result, the effective normal force is closely related to the real contact area. Thus, the modeling of the effective normal force requires the determination of the real contact area in lubricated condition.

During wear, the surface topography in contact is modified due to the plastic deformation of the materials. As an example, Fig. 1 shows a part of the wear track on a CoCrMo alloy disk rubbed by an alumina ball in 0.5 M H_2SO_4 solution. Many scratches and ridges along the sliding direction were found inside the wear track, while the much harder alumina ball had almost no wear. Clearly, the metal disk was plastically deformed and copied the topography of the alumina ball surface in the wear track. For example, the asperities on the ball scratched the alloy to form grooves on the disk and the grooves on the ball wear the metal less and formed ridges on the disk. Note here that generated wear particles transferred and stuck onto the alumina ball surface should be considered as part of the ball surface. In two body sliding contact, the wear surface of the metal disk will be generally conformal to the ball surface especially in the image plane perpendicular to the sliding direction. This explains why it is often observed that the line roughness perpendicular to the sliding direction is high but along the sliding direction the roughness can be very small, as demonstrated in Fig. 1.

It should be noted that in Fig. 1, except the general topography (scratches, grooves and flat surfaces in between), one can find another finer topography which is composed of tiny asperities distributed locally on the walls of the scratches and ridges as well as on the flat surfaces. As demonstrated in Fig. 2, perpendicular to the sliding direction, the two counterparts are getting macroscopically conformal by creating asperity–scratch and groove–ridge couples in the contact. However, the real contacts occurs between the local small asperities on these two conformal surfaces. In tribocorrosion, these small contacting asperities plastically deform and generate wear. Clearly, the real contact area should be determined from the contact between these small asperities. In order to obtain the real contact area, the total contact in Fig. 2(a) should be split into the conformal surfaces (Fig. 2b) and the local asperity contacts (Fig. 2c). After splitting, the two conformal surfaces are theoretically not in direct contact because they are partially separated
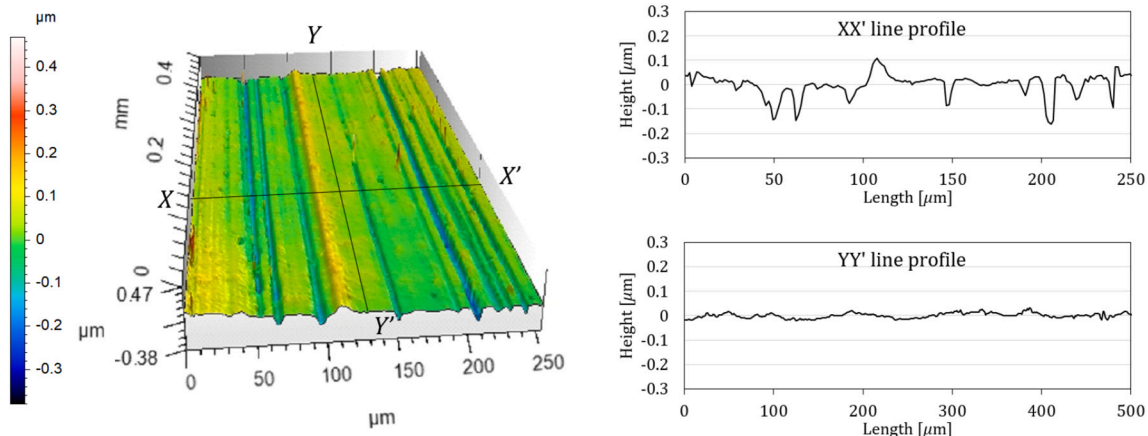

Fig. 1. 3D topography of a typical sliding worn surface on the metal (sliding direction: back to front).
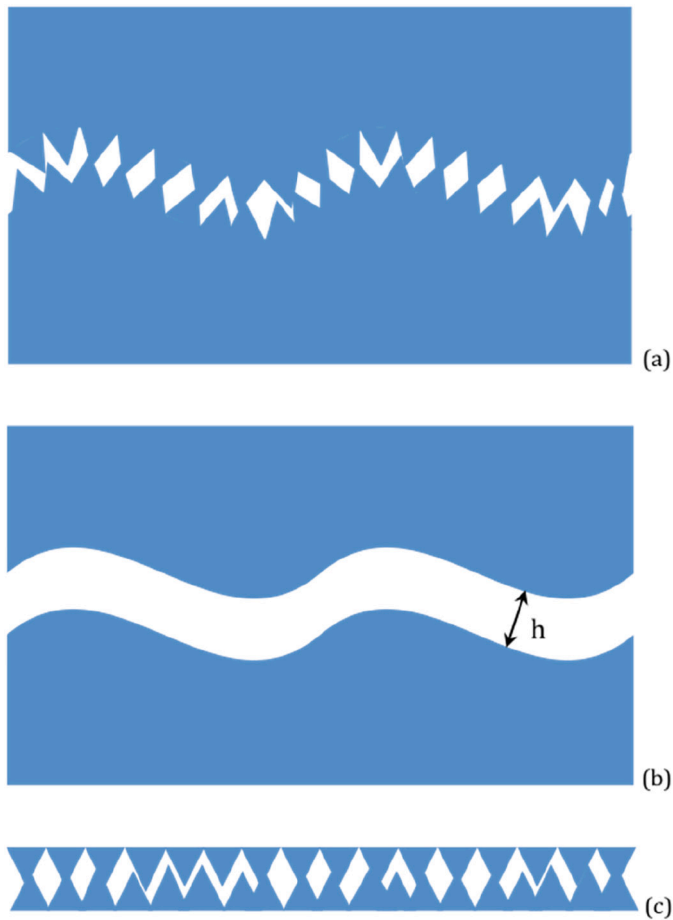
Fig. 2. Schematics of the typical contact during wear taken perpendicular to the sliding direction (sliding direction: back to front): (a) total contact, (b) conformal surfaces without local asperities, (c) local asperity contacts without conformal surfaces.

by the lubricating fluid film. The separation between these two conformal surfaces affects the extent of real contact area between the asperities. This separation can be described using the fluid film thickness h, as shown in Fig. 2(b). To determine the real contact area, the other requirement is the profiles of the local asperities (Fig. 2c). These profiles cannot be directly measured and need to be extracted by, e.g. filtering, from measured global profile as shown in Fig. 2(a).

Once the profile of the local asperities (Fig. 2c) is available, Fig. 3

shows how to describe the fraction of real contact area as opposed to the nominal contact area using the asperities profile. Fig. 3(a) is a typical asperity profile of the wear track after removal of the conformal surfaces, as described in Fig. 2. The lowest point of the surface profile in Fig. 3(a) is set as 0 and the highest point is a. The real contacting level z_0 under loading is between 0 and a in mixed lubricated condition. When z_0 is higher than a, there is no asperity contact (hydrodynamic lubrication) and there is no lubricant in the contact when z_0 is 0 or lower than 0 (non-lubricated). Fig. 3 (b) and (c) show the probability curve and the cumulative probability curve (also called Abbott-Firestone curve [21]) of the asperity profile shown in Fig. 3(a) and from Fig. 3(c), the fraction of the asperity contacting area (real contact area) to the nominal contact area can be extracted from the Abbott-Firestone curve at a certain contacting level, e.g. z_0. Provided the separation (fluid film thickness h) were determined, the effect of this fluid film on the real contact area can be addressed by adding this thickness to the z_0 in order to obtain the new fraction from the Abbott-Firestone curve (Fig. 3c).

2.2. Describing Effective Normal Force Based on Real Contact Area

Following the previous section, in tribological contact, if the real contact is e.g. at level z_0, the asperities higher than level z_0 will be deformed. Assuming the contacting asperities are only under plastic deformation, the local effective normal force here is the force needed to plastically deform the higher asperities into small flats until reaching z_0. The average stress all over the local asperity contacts corresponds to the plastic yield or hardness of the material. Thus, the total effective normal force is linearly proportional to the real contact area, the proportionality being the hardness of the material, as shown in Eq. (3):

$$F_{eff} = HA_{real} \tag{3}$$

In mixed lubricated condition, the total normal force F_n is applied to the total contact area which is the sum of asperity contacts and areas occupied by lubricant. The effective normal force F_{eff} is the force carried only by the asperity contacts (real contact area) and thus the difference between these two forces (F_n–F_{eff}) is the force carried by the lubricant. Therefore, the effective normal force F_{eff} can only be equal or smaller than the total normal force F_n. From Eq. (3), it can be seen that the effective normal force increases with increasing real contact area. When the effective normal force reaches the total normal force, the real contact area is defined as A_n.

$$F_n = HA_n \tag{4}$$

Note that A_n is not necessarily equal to the nominal contact area. The real contact area can be determined from the Abbott-Firestone curve $\Phi(z)$, depending on the real contacting level z_0, as shown in Fig. 4. When the separation is a, there is no asperity contact and all of the total normal
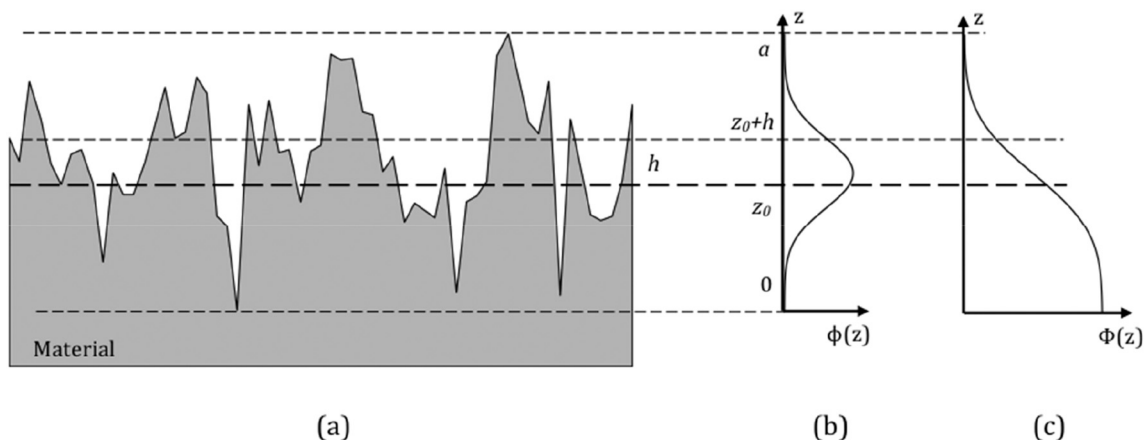

Fig. 3. Schematics of (a) a typical asperity profile, (b) the probability curve and (c) the cumulative probability curve.
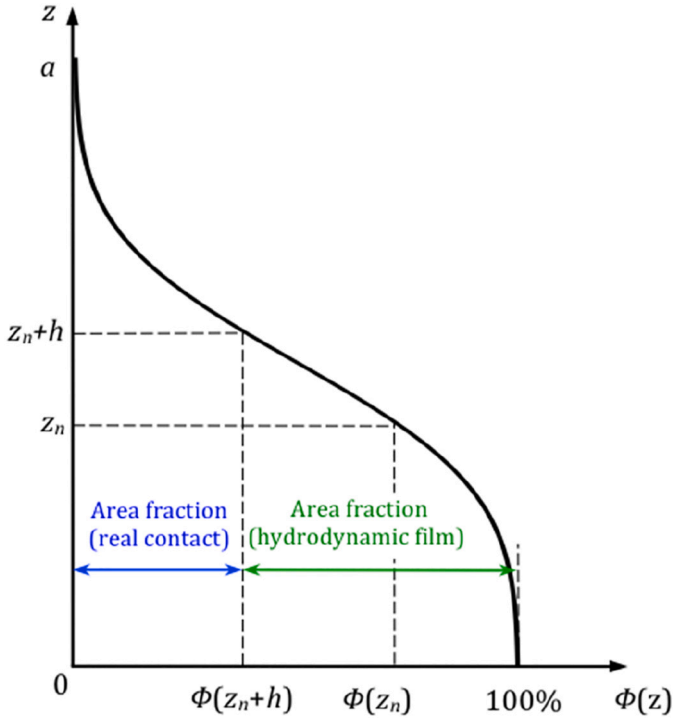
Fig. 4. Determination of the fraction of the real contact area to the total area based on the Abbott–Firestone curve of the asperity profile.

force is carried by the lubricant. With the decrease of the separation, the real contact area increases, thus the F_{eff} also increases. When the separation is z_n, the F_{eff} reaches F_n. From this point on, all of the total normal force is carried by the contacting asperities. In non-lubricated condition, the effective normal force always equals to the total normal force and the real contact area is always A_n. While in lubricated condition, due to the load carrying effect by the lubricant, the real contact will be further separated by h as demonstrated in Fig. 3. As a result, h can be added to z_n to determine the real contacting level in lubricated condition, as shown in Fig. 4.

In Fig. 4, when the separation z is 0, the total contact area equals to the nominal contact area A_{nom} which can be estimated using the Hertzian contact theory as shown in Eq. (5):

$$A_{nom} = \pi \left(\frac{3F_n R'}{4E'} \right)^{2/3} \tag{5}$$

Comparing A_n and A_{nom}, there are two possibilities: (a) when $A_n < A_{nom}$, the effective normal force reaches the total normal force before the real contact level reaches $z = 0$, as shown an example in Fig. 4. This is the situation when little lubricant exists in the deep grooves in Fig. 3(a) and therefore doesn't have any load carrying capability. (b) when $A_n = A_{nom}$, the effective normal force reaches the total normal force only when the real contact level is at $z = 0$. This represents the situation when any lubricant amount in the contact, even a little, will provide load carrying capability.

From Fig. 4, the real contact area and the contact area when F_{eff} reaches F_n can be related to the nominal contact area based on the Abbott-Firestone curve of the asperity profile:

$$\frac{A_{real}}{A_{nom}} = \Phi(z_n + h) \tag{6}$$

$$\frac{A_n}{A_{nom}} = \Phi(z_n) \tag{7}$$

Combining Eqs. (3), (4), (6) and (7), one can obtain the ratio between effective normal force and total normal force according to Eq. (8):

$$\frac{F_{eff}}{F_n} = \frac{A_{real}}{A_n} = \frac{\Phi(z_n + h)}{\Phi(z_n)} \tag{8}$$

From Eq. (8), the model for effective normal force can be developed as shown in Eq. (9) which relates the effective normal force to the total normal force based on the Abbott-Firestone curve of the asperity profile and the fluid film thickness:

$$F_{eff} = F_n \frac{\Phi(z_n + h)}{\Phi(z_n)} \tag{9}$$

Here, z_n should be normal force, material, and asperity profile dependent. In fact, z_n can be determined based on Eqs. (4), (5) and (7). According to Eq. (4), at z_n, the real contact area of the asperities A_n is F_n/H. Incorporating this equation and Eq. (5) into Eq. (7), one can obtain:

$$\Phi(z_n) = \frac{F_n/H}{\pi \left(\frac{3F_n R'}{4E'} \right)^{2/3}} \tag{10}$$

Once $\Phi(z_n)$ is obtained from Eq. (10), z_n can be determined from the Abbott-Firestone curve of the asperity profile, as shown in Fig. 4. Then, the fluid film thickness h can be added to the obtained z_n to get $\Phi(z_n + h)$ from the Abbott-Firestone curve. h is considered as the hydrodynamic film thickness between two smooth surfaces during sliding, as shown between the two conformal surfaces in Fig. 2(b). h can be estimated according to the lubrication theories such as the minimum film thickness equation (Eq. 11) developed by Hamrock and Dowson [10] as already used in many studies to estimate the lubrication effect.

$$h_{min} = 2.8 \left(\frac{u\eta}{E'R'} \right)^{0.65} \left(\frac{F_n}{E'R'^2} \right)^{-0.21} R' \tag{11}$$

where, u is the entraining velocity, $u = (v_{s1} + v_{s2})/2$, η is the viscosity of the solution, E' is the effective Young's modulus, $2/E' = (1 - v_1^2)/E_1 + (1 - v_2^2)/E_2$, R' is the composite radius of curvature, $1/R' = 1/R_1 + 1/R_2$ (for convex surfaces), $1/R' = 1/R_1 - 1/R_2$ (for concave surfaces). v_{s1}, E_1, v_1, R_1 and v_{s2}, E_2, v_2, R_2 are the sliding velocity, Young's modulus, Possion's ratio and radius of the two contacting bodies, respectively.

Once $\Phi(z_n)$ and $\Phi(z_n + h)$ were determined from the corresponding Abbott-Firestone curve, the effective normal force F_{eff} can be obtained using Eq. (9).

2.3. Integrating the New Effective Normal Force Model into the Tribocorrosion Model

Now, the new effective normal force F_{eff} obtained in the previous section can be incorporated into the tribocorrosion model (Eq. 1) by replacing F_n by F_{eff} in order to account for the lubrication effect on tribocorrosion of passive metals, as shown in Eq. (12):

$$V_{tot} = k'_{mech} \frac{F_n}{H} v_s \frac{\Phi(z_n + h)}{\Phi(z_n)} + k'_{chem} \frac{Q_p M v_s}{nF\rho} \left(\frac{F_n}{H} \right)^{0.5} \left(\frac{\Phi(z_n + h)}{\Phi(z_n)} \right)^{0.5} \tag{12}$$

where, k_{mech}' and k_{chem}' are the new mechanical wear factor and chemical wear factors.

This model integrated the lubrication effect into a tribocorrosion model by developing a mechanistic description of the effective normal force. The application of this model requires the extraction of the asperity profile from the total worn surface profile generated in tribocorrosion. However, if it is known that the worn surface follows a certain distribution, the surface profile can thus be described by a known mathematical function instead of requiring the Abbott–Firestone curve of the asperity profile. For example, if the asperities in a worn surface follow a Gaussian distribution, only roughness R_q is needed in order to determine $\Phi(z_n)$ and $\Phi(z_n + h)$. Measuring roughness is usually simpler than obtaining the Abbot-Firestone curve of the surface profiles. The surface profile with Gaussian distribution can be described by Eq. (13)

which is related to an error function erf(z) with z and R_q incorporated.

$$\Phi\left(\frac{z}{R_q}\right) = \frac{1}{2}\left[1 + erf\left(\frac{z}{\sqrt{2}\,R_q}\right)\right] \tag{13}$$

$$erf(z) = \frac{1}{\sqrt{\pi}}\int_{-z}^{z} e^{-x^2}\,dx \tag{14}$$

Based on that, the tribocorrosion model described in Eq. (12) can be modified as:

$$V_{tot} = k'_{mech}\frac{F_n}{H}v_s\frac{1 + erf\left(\frac{z_n+h}{\sqrt{2}\,R_q}\right)}{1 + erf\left(\frac{z_n}{\sqrt{2}\,R_q}\right)} + k'_{chem}\frac{Q_pMv_s}{nF\rho}\left(\frac{F_n}{H}\right)^{0.5}\left(\frac{1 + erf\left(\frac{z_n+h}{\sqrt{2}\,R_q}\right)}{1 + erf\left(\frac{z_n}{\sqrt{2}\,R_q}\right)}\right)^{0.5} \tag{15}$$

This simplifies the application of the model to some situations where the asperity profile follows a Gaussian distribution, an ideal situation not necessarily met in tribocorrosion experiments. Thus Eq. (15) can be used only on the base of a statistical analysis of the surface morphology.

3. Tribocorrosion of a CoCrMo Alloy in H₂SO₄–Glycerol Mixtures

Once the new model was developed, experimental results are needed in order to validate the model. In the literature, tribocorrosion experimental results were mostly presented in absence of the Abbott–Firestone curve of the worn surface profiles. As a consequence, literature data can hardly be used to validate the present model. A previous publication from the authors [22] reported the tribocorrosion of a CoCrMo alloy in 0.5 M H₂SO₄–glycerol mixtures and addressed the lubrication effect on tribocorrosion by varying the viscosity of the mixtures. We measured the worn surface profiles on those CoCrMo samples in order to obtain the Abbott–Firestone curves needed for model validation. Moreover, another set of tribocorrosion experiments was performed under the same experimental conditions but using alumina balls with a quite different initial surface roughness.

3.1. Experimental

The new tribocorrosion experiments were carried out using the same tribometer and ball-on-disk reciprocating configuration as in the previous study [22]. The details of the tribometer have been previously described in [23]. The CoCrMo alloy disk samples used in the previous study [22] were re-polished and details of the chemical composition and microstructure of this high carbon CoCrMo alloy can be found in [15]. The alumina balls used in this study (6 mm in diameter) were from the same supplier as the smooth balls but had surface roughness of 1 μm in R_a. Three 0.5 M H₂SO₄–glycerol mixtures were used in the new tribocorrosion experiments: 0.5 M H₂SO₄, 0.5 M H₂SO₄ with 80 vol% glycerol and 0.5 M H₂SO₄ with 95 vol% glycerol. The viscosity of these three solutions is 1.2, 80.5 and 511.4 mPa s, respectively.

In the PMMA tribocorrosion cell, the CoCrMo disk acts as working electrode together with a platinum counter electrode and a standard mercury sulphate electrode (MSE, 0.658 V with respect to the standard hydrogen electrode). Once the tribocorrosion setup was mounted, the tribocorrosion experiments were performed in the following sequence: (1) leave at open circuit potential (OCP) without rubbing for 5 min, (2) apply the passive potential (0 V_{MSE}) without rubbing for 10 min, (3) rubbing for 30 min with the same applied passive potential, (4) stop rubbing while maintaining the applied passive potential for 5 min, (5) stop the experiment and extract the sample. The stroke length was 5 mm with a constant sliding velocity and the dwell time after each stroke was 0.25 s, which results in the sliding velocity of 20 mm/s at a frequency of 1 Hz. The applied load was 5.6 N.

After the tribocorrosion tests, the topography of the worn surfaces

was measured using a white light interferometer with lateral resolution of 1.3 μm and vertical resolution of 0.1 nm, as shown an example in Fig. 1.

3.2. Results

Fig. 5 shows the variation of the coefficient of friction (CoF) and anodic current during the tribocorrosion tests and optical microscopic images of the worn surfaces after testing. Before rubbing, when the potential switches from OCP to the passive potential (0 V_{MSE}), the anodic current first abruptly increased and then gradually decreased as a consequence of passive film formation. Once the sliding started, the passive film fractured in the contact and, as observed, the anodic current jumped to a much higher value since the metal spontaneously rebuilds the passive film. When sliding stopped, depassivation stopped too and the current dropped back to the initial pre-rubbing value. In the 0.5 M H₂SO₄ solution, the CoF was around 0.3 and it decreased to 0.2 when the glycerol content is 80 vol% and to 0.17 with 95 vol% glycerol. The anodic current, which represents the chemical wear, and the width of the wear track also decreased with increasing glycerol content. These results clearly show the enhanced lubrication induced by the increased viscosity of the solutions. Both the friction and the anodic current were larger than those observed using smooth balls (R_a approximately 20 nm) [22] under the same experimental conditions.

Another observation from the worn surface images (Fig. 5 bdf) in these experiments was that much more scratches were found along the sliding direction inside the wear tracks compared to the worn surfaces rubbed using smooth balls [22]. In addition, the width of the scratches was quite uniform for the three worn surfaces and the density of the scratches seems to be independent of the glycerol content.

Table 1 summarized the friction, wear and surface hardness results. The CoF values were obtained by averaging the friction values all over the rubbing time. Chemical wear and total wear (volume of the wear track) were calculated using the same method described in [15,22] and the mechanical wear was obtained by subtracting the chemical wear from the total wear. Hardness was measured inside and outside of the wear tracks using a Vickers micro hardness tester after the tribocorrosion experiments (applied load 0.98 N and dwell time 15 s). Micro-hardness is considered more appropriate here than nano-indentation or macro hardness as it implies imprint depths of several micrometers corresponding to the characteristic plastic deformation depth found in tribocorrosion experiments [15]. No wear or material transfer (except some sparse debris particles) were found on the alumina balls after test.

Fig. 6 shows the variation of average CoF and total wear rate of the CoCrMo alloy with increasing viscosity of the solutions. Clearly, both of CoF and total wear decreased with increasing viscosity for smooth and rough alumina balls, respectively. The gradual decrease of the CoF, indicates that mixed lubrication regime is prevailing in these tribocorrosion experiments. The friction and wear of the CoCrMo alloy rubbed by rough alumina balls were always higher than those rubbed by the smooth alumina balls in the same solution. The CoF in both conditions follows a good power correlation with the viscosity of the solution. The wear rate of the CoCrMo alloy rubbed by the smooth alumina balls also follows a power correlation with the viscosity of the solution. However, the wear obtained using rough alumina balls doesn't follow a power relation with the viscosity of the solution.

3.3. Determining $\Phi(z_n)$ and $\Phi(z_n + h)$

Once the 3D profile of the worn surfaces was obtained, as shown an example in Fig. 7, line profiles can be extracted from Fig. 7. Due to the small width of the wear tracks tested in 0.5 M H₂SO₄ with 95 vol% glycerol, i.e. only approximately 0.1 mm, three line profiles along the sliding direction with a fixed length of 0.5 mm were extracted inside each wear track from the obtained worn surface 3D profiles, as shown in Fig. 7.
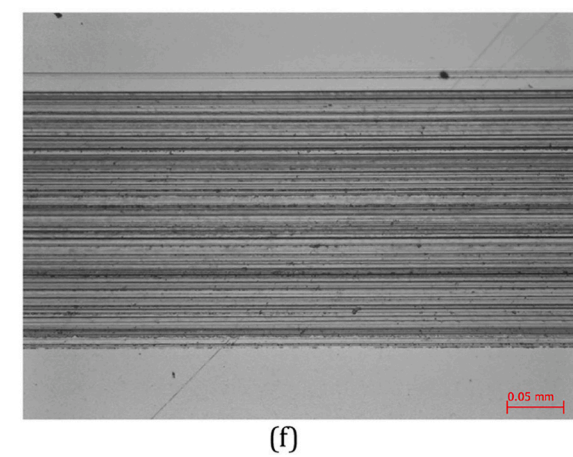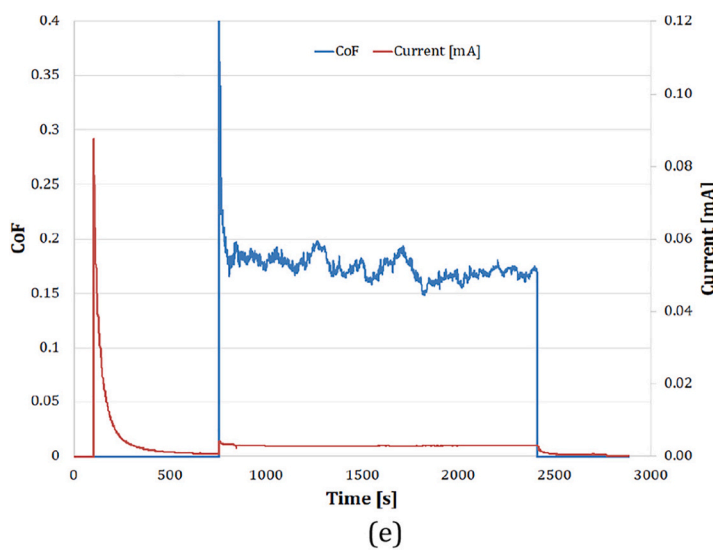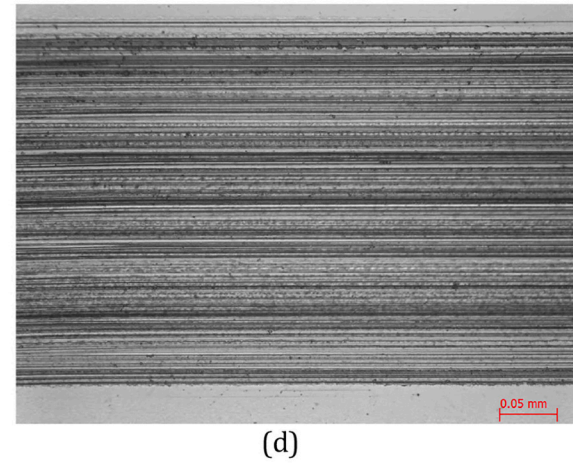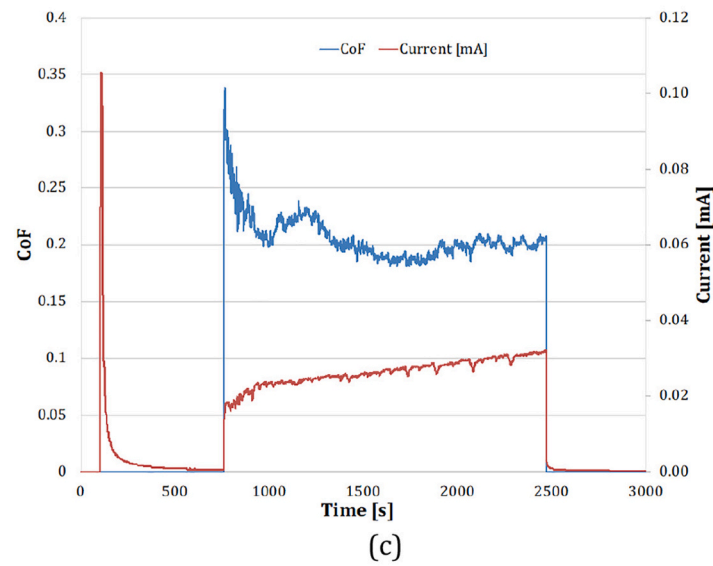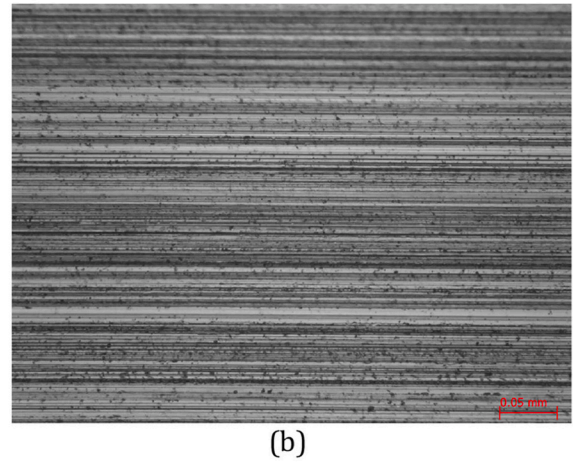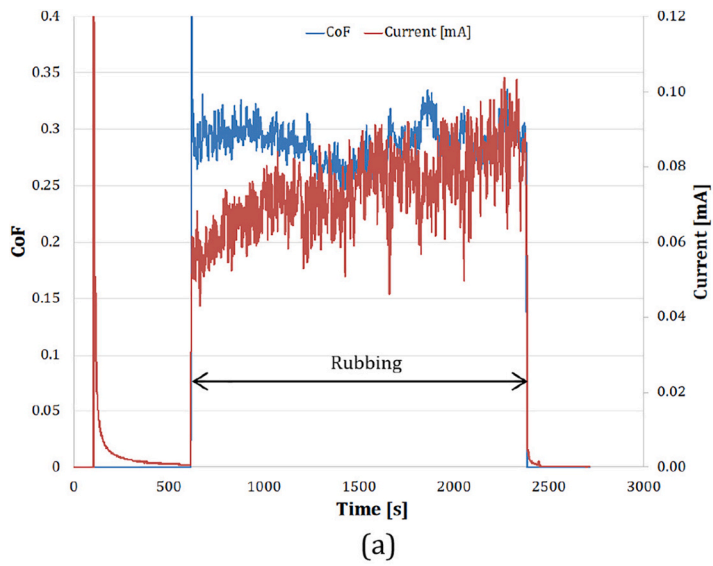
(a)

(b)

(c)

(d)

(e)

(f)

Fig. 5. Coefficient of friction, anodic current and corresponding worn surface of the experiments in 0.5 M H_2SO_4 solutions with different glycerol contents using rough alumina balls (a & b – 0 vol%, c & d – 80 vol%, e & f – 95 vol%).

Table 1
Summary of the results obtained in [22] and from the current tribocorrosion tests.

Ball roughness [μm]	Glycerol content [vol %]	CoF	U_{track} [10^{-3} mm^3]	U_{chem} [10^{-3} mm^3]	U_{mech} [10^{-3} mm^3]	Hardness inside [HV]	Hardness outside [HV]
0.02	0	0.26 ± 0.01	4.67 ± 0.24	3.32	1.34	712 ± 21	475 ± 12
		0.30 ± 0.02	4.72 ± 0.15	3.32	1.40	745 ± 17	490 ± 8
	40	0.29 ± 0.02	2.45 ± 0.05	1.61	0.84	678 ± 17	500 ± 6
		0.27 ± 0.02	2.64 ± 0.05	1.71	0.94	700 ± 23	492 ± 19
	60	0.25 ± 0.01	1.10 ± 0.06	0.80	0.30	607 ± 21	494 ± 4
		0.24 ± 0.02	1.01 ± 0.07	0.74	0.27	638 ± 23	482 ± 22
	80	0.16 ± 0.03	0.43 ± 0.03	0.31	0.12	613 ± 17	480 ± 7
		0.15 ± 0.02	0.48 ± 0.07	0.37	0.12	624 ± 21	489 ± 11
	95	0.09 ± 0.01	0.05 ± 0.02	0.04	0.01	520 ± 19	468 ± 14
		0.11 ± 0.02	0.08 ± 0.01	0.06	0.02	559 ± 16	488 ± 16
1	0	0.29 ± 0.01	8.65 ± 0.06	4.02	4.63	818 ± 48	475 ± 3
	80	0.21 ± 0.03	4.81 ± 0.03	1.39	3.42	737 ± 32	474 ± 12
	95	0.18 ± 0.01	1.90 ± 0.02	0.13	1.77	608 ± 48	492 ± 17
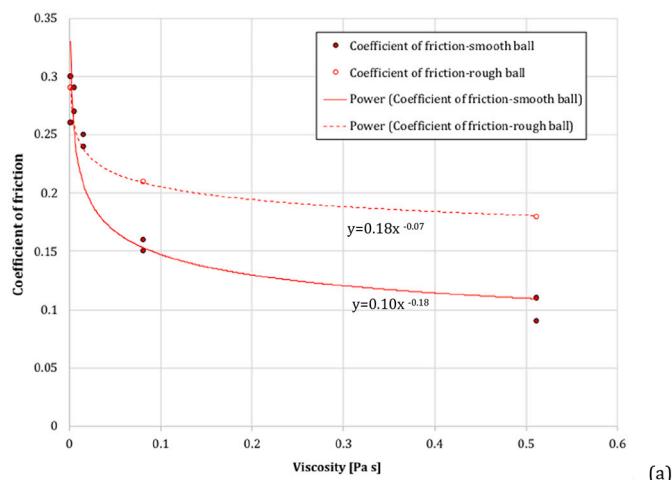
(a)
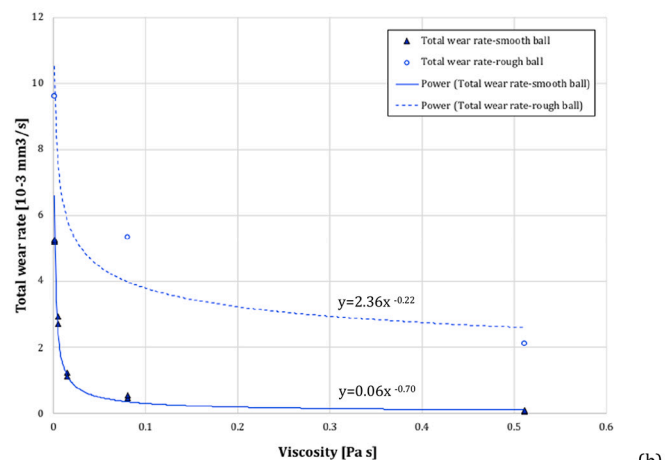
(b)

Fig. 6. Experimental coefficient of friction (a) and total wear rate (b) at different solution viscosities.

Fig. 7. Extracting line profiles from the 3D topography of the wear track (sliding direction: left to right).

One of the extracted line profiles is shown in Fig. 8(a). The large peaks and valleys the conformal surface of which the wavelength varies from approximately 5 μm to 40 μm. In order to get the asperity profile as demonstrated in Fig. 2 which is needed in the model, these large peaks and valleys need to be removed.

The line profile in Fig. 8(a) was filtered by applying a certain cut-off length in order to remove the conformal surface profile in a way same as filtering out waviness in order to obtain roughness according to ISO 4287. A commonly used Gaussian filter was applied. Limited by the
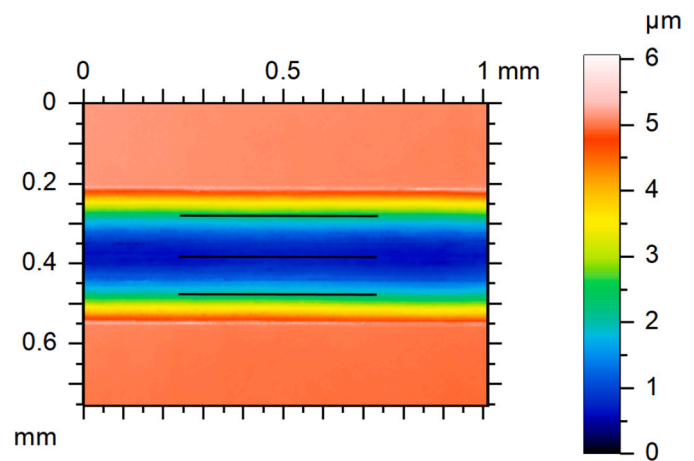
lateral resolution of the interferometer which is 1.3 μm and considering at least five unit lengths as the evaluating length, the cut-off length applied was 10 μm which also falls inside the wavelength of the conformal surface profiles. Fig. 8(b) shows the filtered profile which represents the profile of the asperities shown in Fig. 2(c). Finally, the Abbott-Firestone curve of the filtered profile can be obtained (Fig. 8c). It can be seen from Fig. 8(c) that the asperity profile doesn't follow Gaussian distribution as indicated by the asymmetric histogram of the asperity height distribution. As a result, for applying the tribocorrosion model to these experimental results, Eq. (12) instead of the simplified form (Eq. 15) has to be used.

The $\Phi(z_n)$ and $\Phi(z_n + h)$ were then determined from the Abbott-Firestone curve of each line profile. Firstly, $\Phi(z_n)$ was calculated using Eq. (10). For that, the micro hardness inside the wear tracks after the tribocorrosion experiments shown in Table 1 was used. Then, the obtained $\Phi(z_n)$ value was brought to the corresponding Abbott-Firestone curve of the asperities profile (e.g. Fig. 8c) to get the corresponding z_n value. The hydrodynamic film thickness h was estimated using the minimum hydrodynamic film thickness h_{min} calculated from the Hamrock-Dowson equation [10]. Finally, the corresponding h_{min} value was added to the z_n value and $\Phi(z_n + h)$ was determined from the Abbott-Firestone curve (e.g. Fig. 8c).

Once $\Phi(z_n + h_{min})$ for each profile had been determined from the corresponding Abbott-Firestone curve, A_{real} can be calculated using Eq. (5) and Eq. (6). Then, the ratio between the real contact area and the contact area when F_{eff} reaches F_n in each experiment can be calculated. The results (average value of the three line profiles for each sample) are shown in Table 2. Interestingly, the ratio between A_n and A_{nom} is
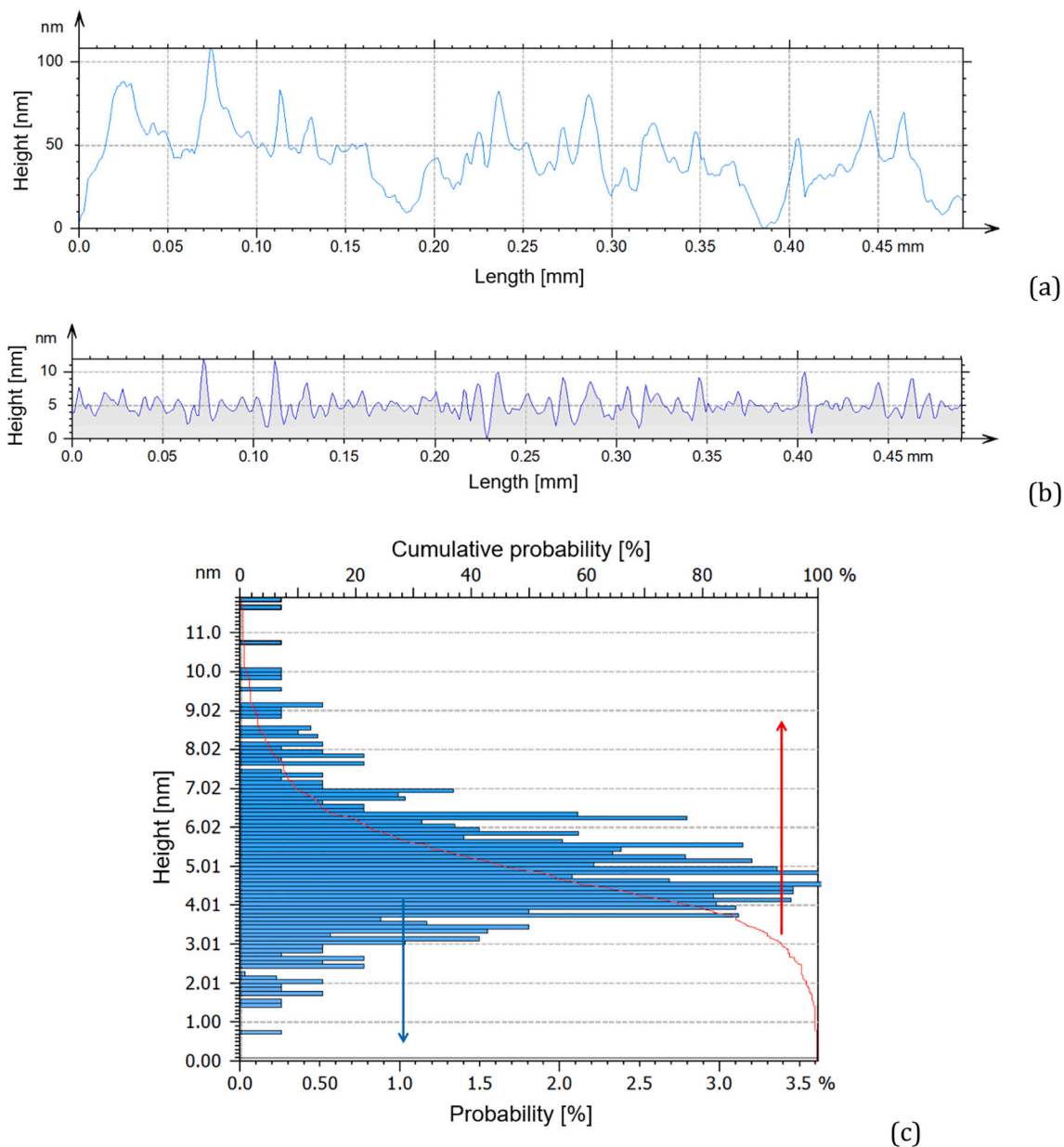
Fig. 8. (a) A line profile from the wear surface tested using smooth alumina balls in 60 vol% glycerol content solution, (b) the filtered profile and (c) the Abbott–Firestone curve of the filtered profile.

Table 2
Summary of the contact area A_n, A_{real} and A_{nom} for each test.

Ball roughness [um]	Glycerol vol%	A_{nom} [10^{-3} mm^2]	A_n [10^{-3} mm^2]	A_n/A_{nom}	A_{real} [10^{-3} mm^2]	A_{real}/A_n
0.02	0	4.469	0.787	17.6%	0.751	95.5%
		4.469	0.752	16.8%	0.737	98.1%
	40	4.469	0.826	18.5%	0.581	70.3%
		4.469	0.8	17.9%	0.693	86.6%
	60	4.469	0.923	20.6%	0.223	24.2%
		4.469	0.878	19.6%	0.313	35.6%
	80	4.469	0.914	20.4%	0.031	3.4%
		4.469	0.897	20.1%	0.089	10%
	95	4.469	1.077	24.1%	0	0%
		4.469	1.002	22.4%	0	0%
1	0	4.469	0.684	15.3%	0.670	97.8%
	80	4.469	0.760	17.0%	0.480	63.2%
	95	4.469	0.921	20.6%	0.223	24.2%

relatively small (around 20%), which indicates the real contact area of asperity junctions due to plastic deformation is just a small fraction of the nominal contact area which considers only elastic deformation. The ratio between A_{real} and A_n, which represents the ratio between F_{eff} and F_n, varied a lot at different glycerol contents, from approximately 95% in 0.5 M H_2SO_4 for both smooth and rough alumina balls to almost 0% in the mixture with 95 vol% glycerol using smooth alumina balls.

4. Comparing Model Predictions with Experimental Results

Once $\Phi(z_n)$ and $\Phi(z_n + h_{min})$ for each worn surface were obtained, the values of each parameter in Eq. (12) for these two sets of experiments are available. Fig. 9 plots the mechanical and chemical wear rates with the variables for these experiments. The average values of $\Phi(z_n + h_{min})/\Phi(z_n)$ obtained from the three line profiles for each sample were used in Fig. 9 and the standard deviations of the variables were also plotted as error bars in the horizontal axes. Despite the large scattering of the $\Phi(z_n + h_{min})/\Phi(z_n)$ values determined from the Abbott-Firestone curves from
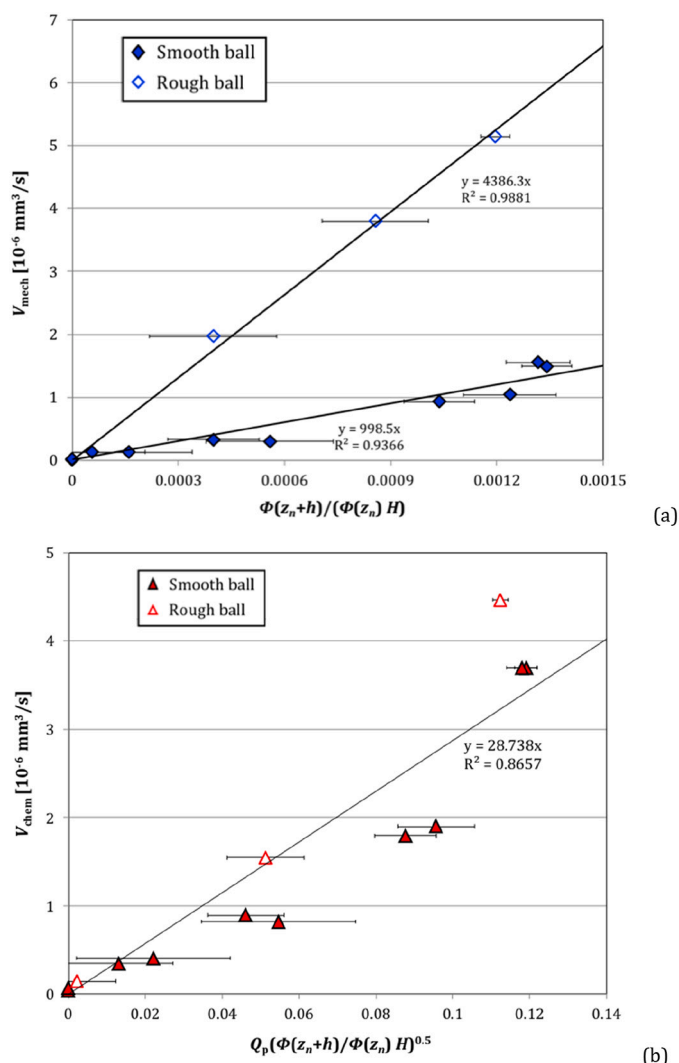
Fig. 9. The correlation between (a) mechanical and (b) chemical wear rates and the group of variables.

three line profiles, clear correlations were found for the mechanical and chemical wear rates.

For mechanical wear, clear deviation of the wear rates tested using rough alumina balls from those tested using smooth alumina balls under the same experimental conditions was observed. However, good linear correlations were found among the wear rates tested using balls with same roughness. For chemical wear, deviation between the alumina balls with different roughness could hardly be observed. The chemical wear rates observed using the rough alumina balls fall quite well inside the linear trend obtained using smooth alumina balls. Only the test in 0.5 M H_2SO_4 using rough balls exhibits slighter higher chemical wear than the linear trend.

From these results, it can be seen that the current two sets of experimental results follow quite well the predictions from the model developed in this study. This supports the validity of this model for predicting the tribocorrosion of passive metals. The effect of ball roughness on the mechanical wear in Fig. 9(a) will be discussed in the next section.

5. Discussion

In the modeling presented in this study, the total contact was conceptually split into the general conformal surfaces and localized asperity contacts. The filtering of the conformal surface in order to

obtain the asperity profile is practically difficult. In this study, it is assumed that the conformal surface profile has a much larger wavelength than the asperity profile, as shown in Fig. 2. From Fig. 5 and Fig. 8 (a), it can be seen that the width of the scratches inside the wear tracks obtained from tests using smooth alumina balls is in the range of several micrometers to several tens micrometer. As a result, the applied cut-off length should be several micrometers in order to remove all the conformal surfaces. Due to the lateral resolution of the profilometer used, a cut-off length of 10 μm was applied. As shown in Fig. 8(b), there are still some remains of the large peaks and valleys, which indicates that the applied cut-off length of 10 μm may not be low enough for these samples. Lower cut-off length can be considered in order to better remove the conformal surface. However, for this higher resolution surface topography measurements are needed. The large values on the horizontal error of the data points in Fig. 9 can also be due to this reason.

From Fig. 9, it can be clearly seen that the mechanical wear presents different proportionality factors between smooth and rough alumina balls while the results using balls with same roughness follow quite good linear correlations. An interesting observation from these two sets of experiments was that large dark wear debris were found outside of the wear track after the tribocorrosion experiments when using the rough alumina balls while very little debris could be observed in case of smooth balls. To explain the different proportionality factors for mechanical wear we propose, the following mechanisms, schematically shown in Fig. 10, based on the concepts originally proposed by Zum Gahr [24].

On one hand, rubbing by smooth balls, the metal disk is contacted with the blunt asperities on the alumina ball surface. As a result, the CoCrMo disk tends to be plastically deformed in a gentle way since the deformation of the metal is spread over a large surface area but over a small depth (Fig. 10). This is a micro-ploughing mechanism as suggested by the relatively smooth worn surface of the CoCrMo alloy tested in 0.5 M H_2SO_4 solution with 95 vol% glycerol as shown in Fig. 11(a). The chemical wear is dominating the total wear (Fig. 9) due to the high ratio between the surface area (approximately proportional to chemical wear) and wear volume (total wear) of the deformed metal (Fig. 10). On the other hand, the rough alumina ball surface is composed of many sharp asperities and therefore these asperities dig deeper into the metal than the blunt asperities of the smooth alumina ball. In this case, a micro-cutting (abrasion) mechanism occurs, as indicated by the narrower but deeper scratches generated by the rough balls (Fig. 11(b)) compared to those formed by the smooth balls (Fig. 11(a)) under the otherwise same experimental condition. Micro-cutting causes the worn surface of the CoCrMo disk to become rougher but also more conformal to the ball surface. As a consequence, a partial transition to micro-ploughing is believed to occur. Similarly, micro-cutting could also happen when using smooth alumina balls due to a certain amount of sharp asperities existing on the smooth alumina ball surface. Therefore, micro-ploughing is the dominating mechanism for the tribocorrosion of this CoCrMo alloy rubbed with smooth alumina balls, while in the case of rubbed with rough alumina balls, micro-cutting mixed with micro-ploughing is believed to be the wear mechanism.

The different mechanical wear but identical chemical wear factors for the smooth and rough balls observed in Fig. 9 could then be explained by the different dominating wear mechanisms. Chemical wear depends on the extent of depassivated surface area Since the width of the wear tracks are just slightly larger in case of rough balls than in case of smooth balls, we expect similar chemical wear rates. This is actually observed in the experimental results shown in Fig. 9(b). On the other hand, according to Fig. 10, the mechanical wear can be significantly promoted by micro-cutting when using rough alumina balls. Filtering of the conformal surfaces by applying a cut-off length of 10 μm, results in considering the big asperities on the rough ball surfaces as conformal topography and being removed. In this way, the mechanical wear due to micro-cutting was ignored in the model prediction. Not surprisingly, experimental mechanical wear was found to be higher than the model
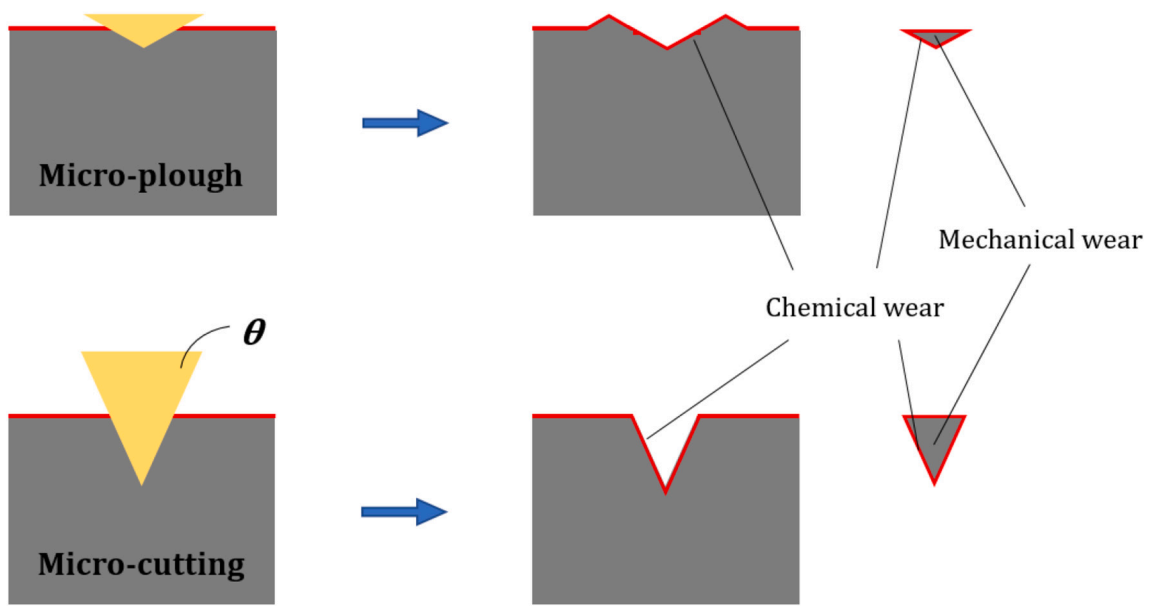
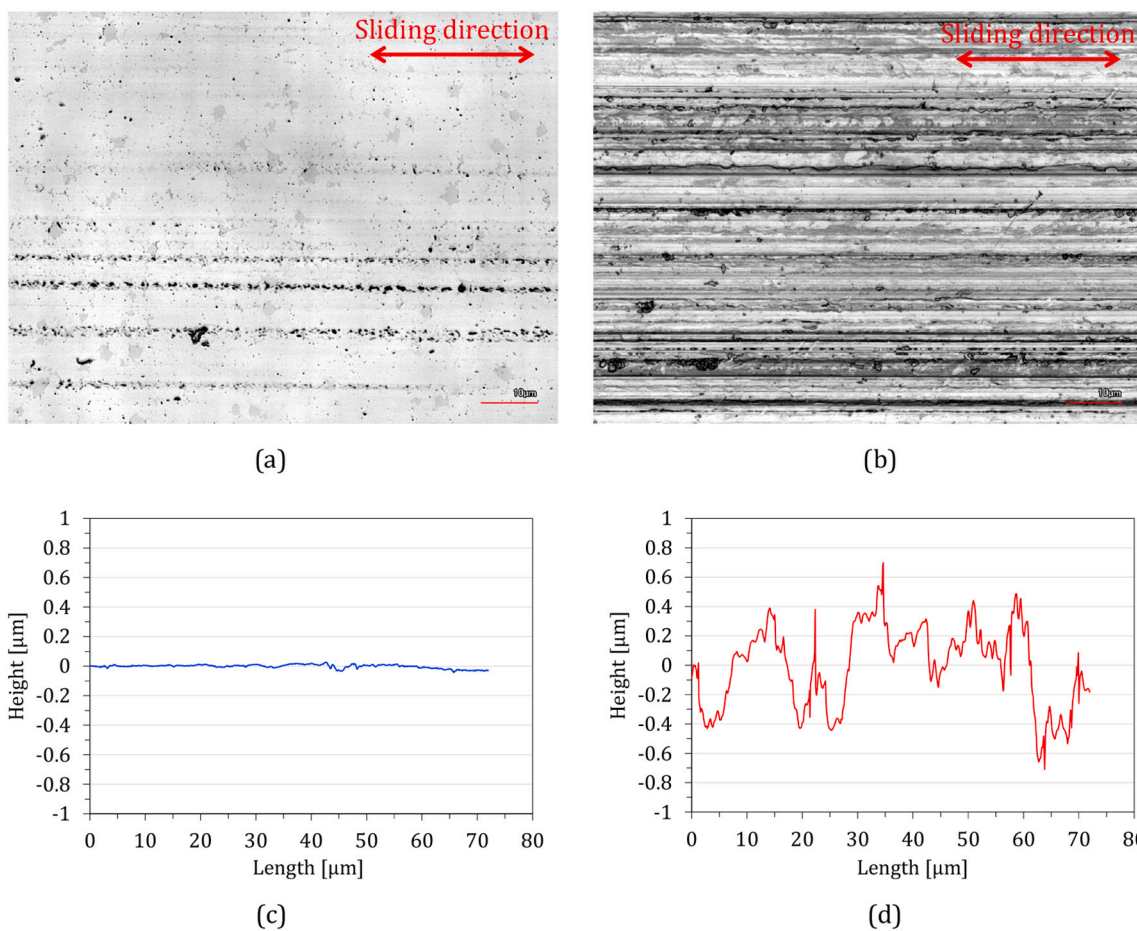**Fig. 10.** Schematic of the two wear mechanisms.

Fig. 11. Comparison of worn surfaces rubbed by (a) smooth alumina ball and (b) rough alumina ball in 0.5 M H_2SO_4 solution with 95 vol% glycerol. (c) and (d) are cross-section profiles perpendicular to the sliding direction of (a) and (b), respectively.

predictions in the case of rough alumina balls. Interestingly, the good linear correlation of mechanical wear with roughness and lubrication factors indicates that wear under micro-cutting conditions may also be influenced by the lubrication effect provided by the solution.

Although the model broadly describes the effect of roughness on chemical and mechanical wear rate it fails to explain the difference

between solutions containing glycerol and glycerol free ones. Indeed, Fig. 9 shows that the wear rates obtained in 0.5 M H$_2$SO$_4$ without glycerol were systematically higher than the trend formed by the data points in H$_2$SO$_4$-glycerol mixtures except the mechanical wear of the CoCrMo disks rubbed with rough alumina balls. It was interpreted in the previous study [22] that the glycerol organic molecules could absorb on the metal surface that affect the tribocorrosion behaviour of the metals by acting as boundary films or changing the grain boundary strength as well as surface energy. This influence is pronounced in both of chemical and mechanical wear when the wear mechanism is micro-ploughing dominated. However, as demonstrated in Fig. 10, if the wear mechanism is micro-cutting dominated, the mechanical wear is much less affected by the absorption than chemical wear since the depth of the micro-cutting could be much larger than the absorption thickness. In fact, this explanation corresponds well to the experimental results (Fig. 9) found in this study.

The presented model allows to predict the materials wastage by chemical and mechanical wear in a given instantaneous situation. Usually tribological and tribocorrosion systems evolve with the progress of wear until a steady state is reached. Clearly the model cannot account alone for this evolution mainly for two reasons. First, plastic deformation may lead to microstructural changes and increase in the number of dislocations in the near-surface zone of the rubbing metal. This provokes usually work hardening and therefore the hardness should be considered as time dependent. Build-up of third bodies is another time dependent effect often encountered in tribological and tribocorrosion contacts. Third bodies may profoundly modify wear mechanisms, surface roughness and stress distribution conditions among other factors. Clearly, such effects are not taken into account by the present "two body" model. Moreover, the surface topography during wear is expected to change gradually due to the plastic deformation of the materials, which is indicated by the running-in and steady state transition found in the wear of MoM artificial hip joints [9,25,26]. The model currently doesn't consider the evolution of the worn surface topography due to the lack of tools to anticipate this evolution. Numerical simulation of the wear surface evolution [27–29] could be a useful tool to be combined with this model in order to predict the instantaneous wear rate due to the evolution of the worn surface topography and to more precisely predict the final wear rates.

Despite these limitations, this new model represents an improvement with respect to the original Cao's model [8]. By considering the correlation between wear and elasto-hydrodynamic lubrication proposed by Dowson equation [9], this previous tribocorrosion model was able to predict with a remarkable precision the wear of hip joints as measured in simulators. However, due to the empirical nature of the Dowson equation [9] its applicability was limited to CoCrMo implants. The present model overcomes this limitation by introducing, a mechanistic correlation determining the wear prevention effectiveness of elasto-hydrodynamic lubrication as a function of roughness. The new model requires only well-defined materials properties (hardness, elasticity, passivation charge). Thus, it can be used to anticipate the behaviour of other materials as alternatives to the CoCrMo alloys widely used so far for hip implants. Moreover, it can be used to assess the wear risk of CoCrMo hip joints in case of significant alterations in surface roughness that may occur during simulator testing or clinical use.

6. Conclusion

(1) A mechanistic tribocorrosion model incorporating lubrication effect was developed by modeling the effective normal force based on worn surface topography.
(2) The tribocorrosion degradation of a CoCrMo alloy was found to be increased when rubbed with rough alumina balls comparing to that rubbed using smooth balls.

(3) The developed model was validated by two sets of the experimental results using smooth and rough alumina balls, respectively.
(4) The model gets rid of empirical correlation between wear and lubrication parameters as used in the previous approach and it can be further verified using more experimental results, e.g. of different materials.
(5) Further development of the model can be focused on the incorporation of boundary film effect and the time evolution of the surface topography during wear with the help of numerical simulations.

Declaration of Competing Interest

Declaration for Journal of Biotribology.

The authors S. Mischler and S. Cao declare not to have any conflict of interest for this purely scientific publication elaborated at EPFL in an academic spirit.

References

[1] A. Neville, Y. Yan, Biotribocorrosion: surface interactions in total joint replacement (TJR), in: D. Landolt, S. Mischler (Eds.), Tribocorrosion of Passive Metals and Coatings, Woodhead Publishing Limited, 2011, pp. 337–367.
[2] J. Villanueva, L. Trino, J. Thomas, D. Bijukumar, D. Royhman, M.M. Stack, M.T. Mathew, Corrosion, tribology, and Tribocorrosion research in biomedical implants: progressive trend in the published literature, J. Bio Tribo-Corrosion 3 (1) (2016) 1.
[3] S. Mischler, A. Igual Munoz, Wear of CoCrMo alloys used in metal-on-metal hip joint: a tribocorrosion appraisal, Wear 297 (2013) 1081–1094.
[4] R.J.K. Wood, Marine wear and tribocorrosion, Wear 376–377 (Part B) (2017) 893–910.
[5] S. Mischler, A. Igual Munoz, Tribocorrosion. Encyclopedia of Interfacial Chemistry, Surface Science and Electrochemistry, Elsevier, 2018. ISBN: 978–0–12-809894-3D.
[6] A. Igual Munoz, N. Espallargas, S. Mischler, Tribocorrosion, Springer, 2020.
[7] S. Cao, S. Mischler, Modeling tribocorrosion of passive metals - a review, Curr. Opinion Solid State Mater. Sci. 22 (2018) 127–141.
[8] S. Cao, S. Guadalupe Maldonado, S. Mischler, Tribocorrosion of passive metals in the mixed lubrication regime: theoretical model and application to metal-on-metal artificial hip joints, Wear 324–325 (2015) 55–63.
[9] D. Dowson, Tribological principles of metal-on-metal hip joint design, Proc. Inst. Mech. Eng. H J. Eng. Med. 220 (2006) 161–171.
[10] B. Hamrock, D. Dowson, Elastohydrodynamic lubrication of elliptical contacts for material of low elastic modulus I-fully flooded conjunction, J. Lubr. Technol. 100 (1978) 236–245.
[11] H.H. Uhlig, Mechanism of fretting corrosion, J. Appl. Mech. 21 (1954) 401–407.
[12] J.F. Archard, Contact and rubbing of flat surfaces, J. Appl. Phys. 24 (1953) 981–988.
[13] S. Mischler, S. Debaud, D. Landolt, Wear-accelerated corrosion of passive metals in tribocorrosion systems, J. Electrochem. Soc. 145 (1998) 750–758.
[14] D. Landolt, S. Mischler, M. Stemp, Electrochemical methods in tribocorrosion: a critical appraisal, Electrochim. Acta 46 (2001) 3913–3929.
[15] S. Guadalupe, S. Mischler, M. Cantoni, et al., Mechanical and chemical mechanisms in the tribocorrosion of a Stellite type alloy, Wear 308 (2013) 213–221.
[16] D. Landolt, S. Mischler, M. Stemp, Electrochemical methods in tribocorrosion: a critical appraisal, Electrochim. Acta 46 (24–25) (2001) 3913–3929.
[17] J. Jiang, M.M. Stack, A. Neville, Modelling the tribo-corrosion interaction in aqueous sliding conditions, Tribol. Int. 35 (10) (2002) 669–679.
[18] C.B. von der Ohe, R. Johnsen, N. Espallargas, Modeling the multi-degradation mechanisms of combined tribocorrosion interacting with static and cyclic loaded surfaces of passive metals exposed to seawater, Wear 269 (7–8) (2010) 607–616.
[19] S. Cao, S. Mischler, Assessment of a recent tribocorrosion model for wear of metal-on-metal hip joints: comparison between model predictions and simulator results, Wear 362–363 (2016) 170–178.
[20] S. Cao, A. Igual Muñoz, S. Mischler, Rationalizing the in-vivo degradation of metal-on-metal artificial hip joints using tribocorrosion concepts, Corrosion 73 (12) (2017) 1510–1519.
[21] M.J. Neale, The Tribology Handbook, Butterworth Heinemann, 1995.
[22] S. Cao, S. Mischler, Tribocorrosion of a CoCrMo alloy in sulfuric acid – glycerol mixtures, Wear 458-459 (2020) 203443.
[23] J. Stojadinovic, D. Bouvet, M. Declercq, et al., Influence of chelating agents on the tribocorrosion of tungsten in sulphuric acid solution, Electrochim. Acta 56 (2011) 7131–7140.
[24] K.-H. Zum Gahr, Microstructure and Wear of Materials, Elsevier, 1987.
[25] C.B. Rieker, R. Schon, R. Konrad, et al., Influence of the clearance on in-vitro tribology of large diameter metal-on-metal articulations pertaining to resurfacing hip implants, Orthop. Clin. N. Am. 36 (2005) 135–142.
[26] D. Dowson, C. Hardaker, M. Flett, et al., A hip joint simulator study of the performance of metal-on-metal joints: part I: the role of materials, J. Arthroplast. 19 (2004) 118–123.

[27] A. Dalmau, A.R. Buch, A. Rovira, J. Navarro-Laboulais, A. Igual Muñoz, Wear model for describing the time dependence of the material degradation mechanisms of the AISI 316L in a NaCl solution, Wear 394-395 (2018) 166–175.

[28] M.S. Uddin, L.C. Zhang, Predicting the wear of hard-on-hard hip joint prostheses, Wear 301 (2013) 192–200.

[29] J. Andersson, A. Almqvist, R. Larsson, Numerical simulation of a wear experiment, Wear 271 (2011) 2947–2952.